Research Article | Vol. 31, No. 21 / 9 Oct 2023 / Optics Express 35200
Optics EXPRESS

Aberration compensation for enhanced holographic particle characterization

KAITLYNN SNYDER AND DAVID G. GRIER*

Department of Physics and Center for Soft Matter Research, New York University, New York, NY 10003, USA
*david.grier@nyu.edu

Abstract: Holographic particle characterization treats holographic microscopy of colloidal particles as an inverse problem whose solution yields the diameter, refractive index and three-dimensional position of each particle in the field of view, all with exquisite precision. This rich source of information on the composition and dynamics of colloidal dispersions has created new opportunities for fundamental research in soft-matter physics, statistical physics and physical chemistry, and has been adopted for product development, quality assurance and process control in industrial applications. Aberrations introduced by real-world imaging conditions, however, can degrade performance by causing systematic and correlated errors in the estimated parameters. We identify a previously overlooked source of spherical aberration as a significant source of these errors. Modeling aberration-induced distortions with an operator-based formalism identifies a spatially varying phase factor that approximately compensates for spherical aberration in recorded holograms. Measurements on model colloidal dispersions demonstrate that phase-only aberration compensation greatly improves the accuracy of holographic particle characterization without significantly affecting measurement speed for high-throughput applications.

1. Holographic particle characterization

Holograms encode a trove of information about objects that scatter light, including their three-dimensional positions, their sizes and shapes, and even clues to their composition. Given some *a priori* knowledge about the nature of the sample, analyzing a hologram can be treated as an inverse problem that is solved by optimizing parameters in the generative model for the image-formation process [1,2]. This inverse-problem approach has been used very successfully to track and characterize micrometer-scale colloidal particles using images captured with holographic video microscopy [1,2]. The precision and speed with which holographic analysis reveals the properties and behavior of individual colloidal particles have inspired new avenues for fundamental research in soft-matter science [3–5] and have created application areas in fields such as biopharmaceuticals [6,7], semiconductor processing [8] and medical diagnostics [9].

The standard implementation of holographic particle characterization uses an in-line holographic microscope [10] of the kind depicted schematically in Fig. 1 to record holograms of colloidal particles. The reference instrument for this study uses a fiber-coupled diode laser (Coherent Cube) operating at a vacuum wavelength of $\lambda = 447$ nm to illuminate the sample. This collimated beam of light interferes with light scattered by particles in the sample volume in the focal plane of an objective lens (Nikon S-Plan Apo, 100× numerical aperture 1.4, oil-immersion). The magnified interference pattern is relayed by a tube lens (200 mm focal length achromat) to a video camera (FLIR Flea 3, USB 3.0, monochrome, 8 bits/pixel) that records its intensity at an effective magnification of 48 nm/pixel.

Features of interest are cropped from the camera's full field of view [11–14] for subsequent analysis [1,13–15]. Figure 1 includes a typical hologram of a 1.5 µm-diameter polystyrene sphere dispersed in water. The inverse-problem analysis involves fitting such an image pixel-by-pixel to predictions of a generative model for the image-formation process. The incident laser beam may

#494593 https://doi.org/10.1364/OE.494593
Journal © 2023 Received 1 May 2023; revised 7 Jul 2023; accepted 25 Aug 2023; published 5 Oct 2023

Optics EXPRESS

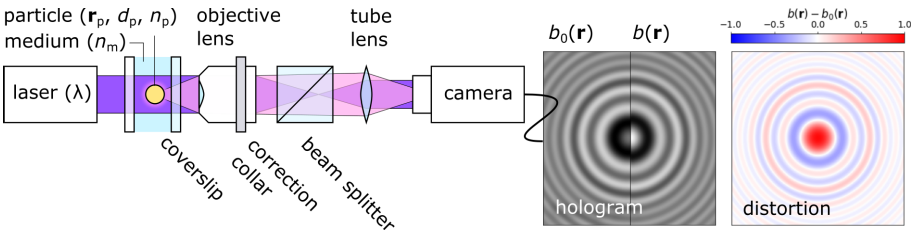

Fig. 1. An in-line holographic microscope illuminates a colloidal particle with a collimated laser beam. Light scattered by particles propagates along with the rest of the illumination through the microscope's optical train to a camera that records its intensity. The resulting hologram ideally is a magnified view of $b_0(\mathbf{r})$, the interference pattern formed by the scattered wave and a plane wave. Non-ideal elements of the optical chain, however, introduce aberrations that produce a distorted hologram, $b(\mathbf{r})$. Analyzing $b(\mathbf{r})$ with the ideal model for $b_0(\mathbf{r})$ introduces systematic errors into estimated parameters.

be modeled as a linearly polarized monochromatic plane wave,

$$\mathbf{E}_0(\mathbf{r}) = E_0\, e^{ikz}\, \hat{x}, \tag{1a}$$

where $k = 2\pi n_m/\lambda$ is the wavenumber of light in a medium of refractive index n_m. A small particle at $\mathbf{r}_p$ scatters a portion of this illumination to position $\mathbf{r}$ in the focal plane,

$$\mathbf{E}_s(\mathbf{r}) = E_0(\mathbf{r}_p)\, \mathbf{f}_s\left(k[\mathbf{r} - \mathbf{r}_p]\right), \tag{1b}$$

where $\mathbf{f}_s(k\mathbf{r})$ is the Lorenz-Mie scattering function for that particle [16–18]. A recorded hologram generally is normalized by a background image to mitigate defects in the illumination [1] so that a suitable generative model for a hologram recorded in the plane $z = 0$ is

$$b(\mathbf{r}) = \left|\hat{x} + e^{-ikz_p}\, \mathbf{f}_s\left(k[\mathbf{r} - \mathbf{r}_p]\right)\right|^2. \tag{1c}$$

For the particular case of a homogeneous spherical scatterer, $\mathbf{f}_s(k\mathbf{r})$ is parameterized by the particle's diameter, d_p, and by its refractive index, n_p, at the imaging wavelength.

Equation (1) has been used to track and characterize colloidal spheres [1], emulsion droplets [19], and gas bubbles [7], and typically yields 2 nm precision for diameter, 2 nm precision for in-plane position, 4 nm precision for axial position and 0.001 precision for refractive index [20]. This performance generally is found to be independent of the particle's height, z_p, above the focal plane [21] over a range that is limited on the low end by the camera's spatial resolution and dynamic range, and on the high end by imaging system's signal-to-noise ratio [22,23]. Efficient software implementations can process 1280 pixel × 1024 pixel holograms at video rates [13], enabling large-population studies and high-throughput applications.

2. Aberration compensation

The accuracy and precision of holographic particle characterization depend on how well the generative model represents the image-formation process. The idealized model in Eq. (1) implicitly assumes aberration-free imaging. Departures from ideal imaging can introduce geometric aberrations that distort the scattered field in a way that is not accounted for by Eq. (1b). Fitting a distorted hologram with the ideal generative model not only slows numerical convergence but also introduces systematic errors into estimates for the particle's position and properties.

Minimizing aberrations through good optical design routinely yields part-per-thousand precision and accuracy for holographic particle tracking and characterization [20], but is not

Optics EXPRESS

always feasible. A holographic microscope may be part of a larger optical train whose components, represented schematically by a beam splitter cube in Fig. 1, may introduce aberrations that cannot be readily corrected in hardware. The aberration correction in commercial objective lenses, furthermore, is only optimized for a medium with a specific refractive index, n_m, and over a limited range of axial positions, z_p. Imaging non-standard samples [19] in large volumes [21] therefore can lead to spurious results.

Previous studies have accounted for the influence of aberrations through detailed modelling of light's passage through the microscope, typically employing path-integral formalism to account for both ray deviations and phase distortions [22–28]. While effective, these methods are computationally intensive, and thus are too slow for many applications. We instead adopt an operator formalism to correct for geometric aberrations that can recover much of the precision and accuracy afforded by an aberration-free instrument while retaining the speed and robustness of the ideal model's implementation.

Because the distortions induced by geometric aberrations preserve a hologram's integrated intensity, they can be described as the action of unitary operators [29,30]. Spherical aberration, in particular, is generated by a non-uniform dilation operator that we model as

$$\hat{D}(x) = 3x\,(1 + x^2)\,\frac{\partial}{\partial x}, \tag{2a}$$

where $x = \rho/\Omega$ is the distance, ρ, from the particle's centroid in the imaging plane relative to the effective aperture of the imaging system, Ω. Referring to Eq. (1), $\left|\mathbf{r} - \mathbf{r}_p\right|^2 = \rho^2 + z_p^2$. For an in-line holographic microscope, the effective aperture depends on the particle's height, z_p, above the focal plane and can be modeled as

$$\Omega(z_p) = \sqrt{2}\,z_p. \tag{2b}$$

The associated unitary operator is

$$\hat{A}(\alpha) = e^{i\alpha}e^{-i\alpha\hat{D}(x)}, \tag{3a}$$

where α quantifies the degree of aberration and where the leading phase factor avoids introducing an overall phase offset. This operator does not distort the collimated reference beam, but introduces both spatial deviations and phase variations to the wavefronts of the scattered wave:

$$\mathbf{E}_s(\mathbf{r}, \alpha) = \hat{A}(\alpha)\,\mathbf{E}_s(\mathbf{r}). \tag{3b}$$

In principle, the aberration operator, $\hat{A}(\alpha)$, could be introduced directly into the generative model in Eq. (1) to account for spherical aberrations in the field scattered by the particle. The exponentiated differential operator, however, significantly increases the time required to evaluate trial holograms. Rather than incurring this computational cost, we instead approximate the effect of spherical aberrations on a general scattered field by applying $\hat{A}(\alpha)$ to the spherical wave scattered by a point particle,

$$\mathbf{f}_s(k\mathbf{r}) \approx \frac{e^{-ikr}}{kr}\,\hat{x}. \tag{4}$$

The principal effect is to multiply the input wave by a spatially-varying phase factor,

$$\mathbf{E}_s(\mathbf{r}, \alpha) \approx \exp\left(-i\,\alpha\,R_4^0\left(\frac{r}{\sqrt{2}z_p}\right)\right)\mathbf{E}_s(\mathbf{r}), \tag{5a}$$

where

$$R_4^0(x) = 1 - 6x^2 + 6x^4, \tag{5b}$$

is the Zernike polynomial that commonly is associated with the wavefront error or phase distortion due to spherical aberration [31]. The form of the dilation operator in Eq. (2) was chosen with this outcome in mind.

Optics EXPRESS

Equation (5) omits distortions of the amplitude profile of the scattered wave due to spatial deviations of the scattered rays. The entire result, furthermore, strictly pertains only to Rayleigh scatterers, which are much smaller than the wavelength of light. Nevertheless, the functional form of Eq. (5) is appealing because the multiplicative phase correction can be incorporated into the generative model at virtually no computational cost and thus is suitable for real-time applications. The aberration coefficient, α, can be treated as an instrumental calibration constant for routine measurements. Allowing α to vary during fitting can account at least approximately for effects of aberrations that are neglected by a phase-only correction, potentially improving estimation overall.

3. Holographic particle characterization with aberration compensation

The data in Fig. 2 illustrate the dramatic improvement in holographic particle characterization that can be obtained through phase-only aberration compensation with Eq. (5). These data were acquired for two 1.5 µm-diameter silica spheres (Bangs Labs, catalog SS04001) dispersed in water and trapped at $z_p = 20\,\mu$m above the focal plane in a pair of holographic optical tweezers [32]. The dispersion is contained in a 50 µm-thick sample chamber formed by sealing a #1.5 glass coverslip to the surface of a glass microscope slide. The sample is mounted on the stage of the reference holographic microscope [21].

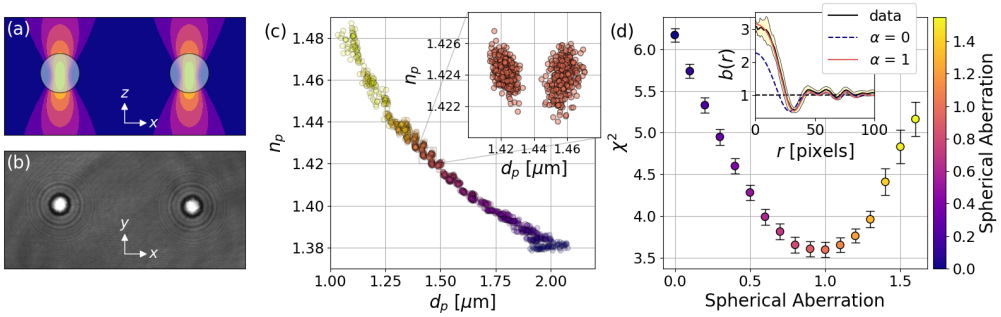

Fig. 2. Experimental demonstration of aberration correction for holographic particle characterization. (a) Schematic representation of two colloidal spheres localized in holographic optical traps. (b) Typical hologram of two 1.5 µm-diameter silica spheres optically trapped in water. (c) Estimates for the diameter, d_p, and refractive index, n_p, obtained by fitting 314 holograms such as the example in (a) to Eq. (5) with different values for the spherical aberration coefficient, α. Each data point reflects the properties of one particle in one hologram and is colored by the value of α used for the fit. Inset: Characterization results for the optimal value, $\alpha = 1$. (d) Reduced χ^2 statistic for fits to Eq. (5) as a function of α. Inset: Radial profile of typical fit showing that aberration compensation substantially improves agreement with measured data at small r.

Optical traps at a vacuum wavelength of 1070 nm (IPG Photonics, YLR-10-LP) are directed into the microscope's objective lens with a dichroic beamsplitter (Thorlabs, DMSP820B) placed between the objective lens and the tube lens. Both the beamsplitter and an infrared filter mounted after the tube lens prevent stray trapping light from reaching the camera. This arrangement allows for independent three-dimensional micromanipulation of multiple colloidal particles with simultaneous tracking and characterization at video rates [21].

The cost of integrating optical tweezers with the holographic microscope is that imaging light must pass through the beamsplitter and the filter, both of which deviate and delay non-paraxial rays. The resulting spherical aberration can be mitigated, in principle, through hardware modifications, for example by deliberately introducing compensating aberrations with the correction collar on the objective lens. In practice, however, such manual optimization is labor-intensive and

Optics EXPRESS

error-prone. Accounting for aberrations through the analytical pipeline is both easier and more general, and can be exceptionally effective.

The raw data set for Fig. 2 consists of 314 video frames of the two optically immobilized particles. These holograms are analyzed by optimizing $\mathbf{r}_p$, d_p and n_p in a generative model with phase-only aberration correction using fixed values for the spherical aberration coefficient that range from $\alpha = 0$ to $\alpha = 1.6$. Each data point in Fig. 2(c) represents the diameter, d_p, and refractive index, n_p, of one of the particles obtained from one of the frames, using the value for α that is indicated by the symbol's color.

Without aberration compensation, the two particles' characterization results form a single cluster in the d_p-n_p plane with a mean diameter, $d_p = 1.99 \pm 0.5\,\mu\text{m}$, that is 30 % larger than expected. The associated estimate for the particles' refractive index, $n_p = 1.380 \pm 0.001$, is significantly smaller than the value of 1.42 expected for colloidal silica [33–35]. Although the uncertainties in the estimated values are small, the large χ^2 statistic for the fits, $\chi^2 = 6.1$, suggests that their accuracy may not be as good as their precision.

As Fig. 2(d) shows, fit quality improves smoothly to $\chi^2 = 3.5$ as the spherical aberration coefficient is increased from $\alpha = 0$ to the optimal value for this instrument, $\alpha = 1.0$. The typical profile plotted in the inset to Fig. 2(d) illustrates that much of the improvement appears at small r. Without aberration compensation, fits tend to prioritize agreement at large r, where more pixels contribute to χ^2 and where the influence of spherical aberration is most pronounced.

Compensating for aberrations coalesces the two particles' characterization results into a pair of well-resolved clusters, one for each particle, as can be seen in the inset to Fig. 2(c). When analyzed in this way, both particles have mean refractive indexes that are consistent with $n_p = 1.424 \pm 0.001$, which also is consistent with expectations for Stöber-synthesized silica. The two particles have estimated diameters of $d_p = 1.423 \pm .003\,\mu\text{m}$ and $(1.458 \pm 0.003)\,\mu\text{m}$, both of which are resolved to within 3 nm and both of which are consistent with the manufacturer's specification for the population-average diameter. The uncertainties in these values are computed as standard deviations for the two clusters of measurements. Additionally, each fit has a numerical uncertainty obtained from the dependence of the χ^2 statistic on the parameters given the holograms' estimated signal-to-noise ratio. The mean fit uncertainties for these data sets are $\sigma_d = 1.5\,\text{nm}$ for the diameter and $\sigma_n = 540\,\text{ppm}$ for the refractive index, both of which are consistent with the standard deviations of the measurements. Uncertainties in the individual fits therefore are consistent with the statistical uncertainties in the particles' properties, which suggests that the fit uncertainties accurately reflect the measurements' precision and accuracy.

The experimental results in Fig. 3 build on this theme by demonstrating that phase-only aberration compensation with Eq. (5a) improves the accuracy of holographic particle characterization for particles with substantially different characteristics. The sample in this case consists of four different types of particles: two sizes of polystyrene spheres, (1) $d_p = 1.0\,\mu\text{m}$ (ThermoScientific, catalog 5100B) and (2) $d_p = 3.2\,\mu\text{m}$ (Interfacial Dynamics, product 1-3000), and two sizes of silica spheres, (3) $d_p = 1\,\mu\text{m}$ (Polysciences, catalog 24326) and (4) $d_p = 3\,\mu\text{m}$ (Bangs Labs, catalog SS05N). Polystyrene has a refractive index around $n_p = 1.6$, which is substantially higher than that of silica.

One particle of each type is optically trapped at a fixed location in the field of view, as shown by the example hologram in Fig. 3(a). For all four particle types, the positive spherical aberration introduced by the optical trapping system causes the standard analysis based on Eq. (1) to overestimate the diameter and underestimate the refractive index. These characterization results are plotted as violet symbols in Fig. 3(b). Accounting for spherical aberration with Eq. (5) substantially revises the estimates, with $\alpha = 1.0$ yielding the results plotted as orange symbols.

Results for the four particles are compared with population-average values obtained for each of the four populations of particles using a commercial holographic particle characterization instrument (Spheryx, xSight) that are plotted as red circles in Fig. 3(b). Each of these ground-truth measurements was obtained with roughly 1000 particles. Error bars represent the populations'

Optics EXPRESS

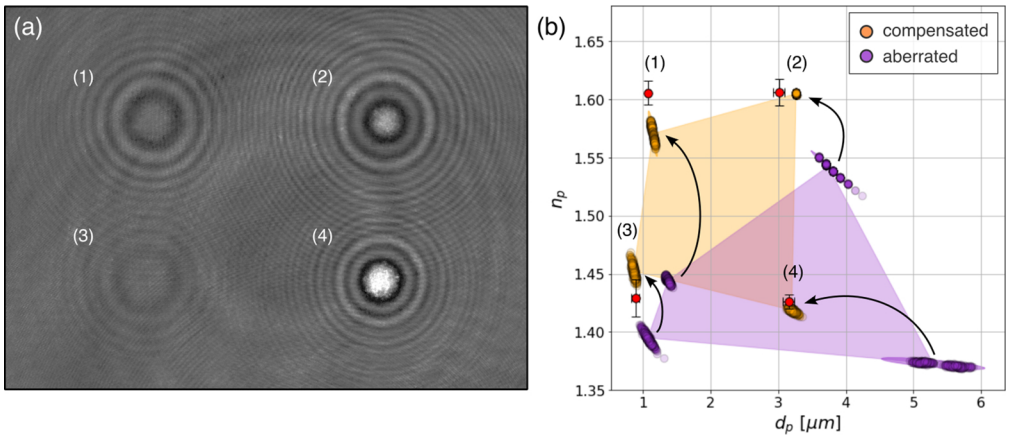

Fig. 3. (a) Typical hologram of four colloidal spheres localized in holographic optical traps: (1) 1 µm-diameter polystyrene, (2) 3 µm-diameter polystyrene, (3) 1 µm-diameter silica, (4) 3 µm-diameter silica. (b) Correcting for spherical aberration improves characterization results. Purple plot symbols show fit values for the diameter, d_p, and refractive index, n_p, for each of the four particles obtained without aberration compensation. Each cluster of points consists of 500 measurements. Orange symbols show results obtained from the same holograms using phase-only aberration compensation described by Eq. (5). The aberration parameter is treated as a fixed calibration constant, $\alpha = 1$. For all four types of particles, aberration correction corrects estimates into reasonable agreement with population-averaged values, which serve as the ground truth (red symbols). Arrows indicate how aberration compensation corrects each particle's characterization results.

Table 1. Summary of results for (a) the diameter, d_p, and (b) refractive index, n_p, for the four particles presented in Fig. 3. Results are obtained both without aberration compensation and also with phase-only aberration compensation. These values are compared with population averages obtained by analyzing the same types of particles with an aberration-free commercial instrument (xSight), which serve as the ground truth. The improvement in accuracy due to aberration compensation is presented relative to the error of the aberrated values.

(a) Diameter [µm]

particle	aberrated	compensated	xSight	Δ accuracy [%]
(1)	1.372(23)	1.148(22)	1.073(23)	75
(2)	3.739(84)	3.265(2)	3.013(83)	68
(3)	1.072(42)	0.866(19)	0.888(63)	88
(4)	5.292(247)	3.202(35)	3.154(83)	98

(b) Refractive Index

particle	aberrated	compensated	xSight	Δ accuracy [%]
(1)	1.444(2)	1.570(6)	1.605(10)	78
(2)	1.542(4)	1.605(1)	1.606(11)	98
(3)	1.395(4)	1.452(5)	1.429(16)	32
(4)	1.373(2)	1.419(1)	1.426(6)	87

standard deviations. Table 1 summarizes single-particle characterization results with and without phase-only aberration compensation and compares these with the ground-truth values for the populations.

Optics EXPRESS

Improvements in accuracy due to aberration compensation are computed as the reduction in the absolute difference of the single-particle result from the population average relative to the uncompensated difference. Individual particles drawn from a population may differ from the mean, in much the same way that the two particles in Fig. 2 differ from each other. Discrepancies between xSight results for the populations and results for the specific particles in Fig. 3 might reflect this underlying variability. More likely, they reflect limitations in the ability of the phase-only model embodied in Eq. (5) to fully compensate for aberrations, particularly when the aberration coefficient, α, is treated as a fixed instrumental parameter.

Small improvements in the agreement with ground-truth values can be achieved by allowing α to vary in each fit. The effective aperture, Ω, similarly can be treated as an adjustable parameter. Beyond being poorly motivated, however, these expedients also increase the likelihood that a fit will fail to converge.

4. Discussion

The experimental results in Sec. 3 illustrate how effectively the simplified phase-factor model introduced in Eq. (5) can compensate for spherical aberration in holographic particle characterization, yielding substantial gains in accuracy with minimal computational cost. Improved agreement between the model and the data furthermore means that fewer iterations are required to achieve convergence. Fitting the data in Fig. 3 requires 10 % less time with Eq. (5) than with the ideal model in Eq. (1). Fitting aberration-free holograms would be faster still, were such holograms available. When spherical aberration is unavoidable, or when its presence cannot be discounted *a priori*, phase-only compensation with Eq. (5) provides an efficient and effective alternative to a more rigorous analysis [25], including the operator-based approach in Eq. (3), and therefore is suitable for real-time and high-throughput applications. The measured value of the spherical-aberration coefficient, α, furthermore can be used to diagnose and correct instrumental problems.

Phase-only aberration compensation also may be helpful for tracking and characterizing aspherical and inhomogeneous particles using the effective-sphere approximation [35]. How well aberration compensation works for such non-ideal particles may be difficult to assess unless model systems can be identified whose ground-truth properties can be independently established.

While the present study has focused on spherical aberration, unitary operators also should be useful for describing other geometric aberrations. Operator-based aberration compensation appears not to have been widely discussed, despite the benefits of speed and efficacy illustrated by the present study. The specific form for the spherical-aberration operator Eq. (2) and Eq. (3) was developed phenomenologically; a more rigorous formulation might perform even better.

Funding. National Science Foundation (DMR-0922680, DMR-1420073, DMR-2104837).

Disclosures. D.G.G. is a founder of Spheryx, Inc., which manufactures instrumentation for Holographic Particle Characterization, including the xSight used for this study.

Data availability. Data underlying the results presented in this paper are not publicly available at this time but may be obtained from the authors upon reasonable request.

References

1. S.-H. Lee, Y. Roichman, G.-R. Yi, S.-H. Kim, S.-M. Yang, A. Van Blaaderen, P. Van Oostrum, and D. G. Grier, "Characterizing and tracking single colloidal particles with video holographic microscopy," Opt. Express **15**(26), 18275–18282 (2007).
2. C. Martin, L. E. Altman, S. Rawat, A. Wang, D. G. Grier, and V. N. Manoharan, "In-line holographic microscopy with model-based analysis," Nat. Rev. Methods Primers **2**(1), 83 (2022).
3. Y. Roichman, B. Sun, A. Stolarski, and D. G. Grier, "Influence of nonconservative optical forces on the dynamics of optically trapped colloidal spheres: the fountain of probability," Phys. Rev. Lett. **101**(12), 128301 (2008).
4. C. Wang, H. Shpaisman, A. D. Hollingsworth, and D. G. Grier, "Celebrating soft matter's 10th anniversary: Monitoring colloidal growth with holographic microscopy," Soft Matter **11**(6), 1062–1066 (2015).

Optics EXPRESS

5. R. W. Verweij, S. Ketzetzi, J. De Graaf, and D. J. Kraft, "Height distribution and orientation of colloidal dumbbells near a wall," Phys. Rev. E **102**(6), 062608 (2020).
6. P. N. O. Kasimbeg, F. C. Cheong, D. B. Ruffner, J. M. Blusewicz, and L. A. Philips, "Holographic characterization of protein aggregates in the presence of silicone oil and surfactants," J. Pharm. Sci. **108**(1), 155–161 (2019).
7. A. Winters, F. C. Cheong, M. A. Odete, J. Lumer, D. B. Ruffner, K. I. Mishra, D. G. Grier, and L. A. Philips, "Quantitative differentiation of protein aggregates from other subvisible particles in viscous mixtures through holographic characterization," J. Pharm. Sci. **109**(8), 2405–2412 (2020).
8. F. C. Cheong, P. Kasimbeg, D. B. Ruffner, E. H. Hlaing, J. M. Blusewicz, L. A. Philips, and D. G. Grier, "Holographic characterization of colloidal particles in turbid media," Appl. Phys. Lett. **111**(15), 153702 (2017).
9. K. Snyder, R. Quddus, A. D. Hollingsworth, K. Kirshenbaum, and D. G. Grier, "Holographic immunoassays: direct detection of antibodies binding to colloidal spheres," Soft Matter **16**(44), 10180–10186 (2020).
10. J. Sheng, E. Malkiel, and J. Katz, "Digital holographic microscope for measuring three-dimensional particle distributions and motions," Appl. Opt. **45**(16), 3893–3901 (2006).
11. B. J. Krishnatreya and D. G. Grier, "Fast feature identification for holographic tracking: The orientation alignment transform," Opt. Express **22**(11), 12773–12778 (2014).
12. M. D. Hannel, A. Abdulali, M. O'Brien, and D. G. Grier, "Machine-learning techniques for fast and accurate feature localization in holograms of colloidal particles," Opt. Express **26**(12), 15221–15231 (2018).
13. L. E. Altman and D. G. Grier, "CATCH: Characterizing and tracking colloids holographically using deep neural networks," J. Phys. Chem. B **124**, 1602–1610 (2020).
14. L. E. Altman and D. G. Grier, "Machine learning enables precise holographic characterization of colloidal materials in real time," Soft Matter **19**(16), 3002–3014 (2023).
15. A. Yevick, M. Hannel, and D. G. Grier, "Machine-learning approach to holographic particle characterization," Opt. Express **22**(22), 26884–26890 (2014).
16. C. F. Bohren and D. R. Huffman, *Absorption and Scattering of Light by Small Particles* (John Wiley & Sons, 2008).
17. M. I. Mishchenko, L. D. Travis, and A. A. Lacis, *Scattering, Absorption, and Emission of Light by Small Particles* (Cambridge University, 2002).
18. G. Gouesbet and G. Gréhan, *Generalized Lorenz-Mie Theories* (Springer, 2011).
19. H. Shpaisman, B. Jyoti Krishnatreya, and D. G. Grier, "Holographic microrefractometer," Appl. Phys. Lett. **101**(9), 091102 (2012).
20. B. J. Krishnatreya, A. Colen-Landy, P. Hasebe, B. A. Bell, J. R. Jones, A. Sunda-Meya, and D. G. Grier, "Measuring Boltzmann's constant through holographic video microscopy of a single colloidal sphere," Am. J. Phys. **82**(1), 23–31 (2014).
21. M. J. O'Brien and D. G. Grier, "Above and beyond: holographic tracking of axial displacements in holographic optical tweezers," Opt. Express **27**(18), 25375–25383 (2019).
22. C. Martin, B. Leahy, and V. N. Manoharan, "Improving holographic particle characterization by modeling spherical aberration," Opt. Express **29**(12), 18212–18223 (2021).
23. F. Goméz, R. S. Dutra, L. B. Pires, G. R. d. S. Araújo, B. Pontes, P. A. Maia Neto, H. M. Nussenzveig, and N. B. Viana, "Nonparaxial Mie theory of image formation in optical microscopes and characterization of colloidal particles," Phys. Rev. Appl. **15**(6), 064012 (2021).
24. H. W. Moyses, B. J. Krishnatreya, and D. G. Grier, "Robustness of Lorenz-Mie microscopy against defects in illumination," Opt. Express **21**(5), 5968–5973 (2013).
25. R. Alexander, B. Leahy, and V. N. Manoharan, "Precise measurements in digital holographic microscopy by modeling the optical train," J. Appl. Phys. **128**(6), 060902 (2020).
26. T. Olivier, D. Brault, S. Joshi, T. Brard, A. Brodoline, L. Méès, and C. Fournier, "Effects of some model approximations in the reconstructions of digital in-line holograms: simulations, experiments on calibrated objects and model refinement assessment," in *Unconventional Optical Imaging III*, vol. 12136 (SPIE, 2022), pp. 7–17.
27. D. G. Sirico, L. Miccio, Z. Wang, P. Memmolo, W. Xiao, L. Che, L. Xin, F. Pan, and P. Ferraro, "Compensation of aberrations in holographic microscopes: main strategies and applications," Appl. Phys. B **128**(4), 78 (2022).
28. D. Brault, T. Olivier, F. Soulez, S. Joshi, N. Faure, and C. Fournier, "Accurate unsupervised estimation of aberrations in digital holographic microscopy for improved quantitative reconstruction," Opt. Express **30**(21), 38383–38404 (2022).
29. J. Visser, N. J. Zelders, and G. Nienhuis, "Wave description of geometric modes of a resonator," J. Opt. Soc. Am. A **22**(8), 1559–1566 (2005).
30. J. Visser and G. Nienhuis, "Spectrum of an optical resonator with spherical aberration," J. Opt. Soc. Am. A **22**(11), 2490–2497 (2005).
31. M. Born and E. Wolf, *Principles of Optics* (Elsevier, 2013).
32. D. G. Grier, "A revolution in optical manipulation," Nature **424**(6950), 810–816 (2003).
33. I. H. Malitson, "Interspecimen comparison of the refractive index of fused silica," J. Opt. Soc. Am. **55**(10), 1205–1209 (1965).
34. F. C. Cheong, K. Xiao, D. J. Pine, and D. G. Grier, "Holographic characterization of individual colloidal spheres' porosities," Soft Matter **7**(15), 6816–6819 (2011).
35. M. A. Odete, F. C. Cheong, A. Winters, J. J. Elliott, L. A. Philips, and D. G. Grier, "The role of the medium in the effective-sphere interpretation of holographic particle characterization data," Soft Matter **16**(4), 891–898 (2020).